Controlled Air Jet Blowing for the Homogenization of Compression Bump Air Intake Flows

Markus Rütten*

*German Aerospace Center (DLR), Institute of Aerodynamics and Flow Technology, Department of High Speed Configurations, 37073 Göttingen markus.ruetten@dlr.de

†Corresponding author

Abstract

In the development of new fighter aircraft compression bump engine air intakes play a major role, since they contribute to the reduction of radar cross section due to their geometrical shape. However, in regard to aerodynamic characteristics in comparison to Pitot air intakes, the compression bump geometry has to be designed optimally in order to guarantee high total pressure recoveries by displacing the incoming boundary layer so far outwards that only high momentum flow enters the air intake channel. The objective of the compression bump air intake design and the following air intake channel is to achieve the highest possible total pressure recovery at the aerodynamic interface plane to the engine, along with a homogeneous flow distribution with the lowest possible flow distortion. In most cases certain design Mach numbers, engine mass flows and angles of attack are addressed in the intake design and optimization process. However, angles of attack and, equally important, angles of side slip are changing rapidly during maneuver flights. This results into non uniform and asymmetric onflow in front of the air intake, under certain conditions, in strong asymmetric vortical flow separation. Eventually, all that accumulates to an asymmetrically shifted and concentrated total pressure loss region at the aerodynamics interface plane to the engine, which has a significantly negative impact on engine performance itself. Therefore, active flow control methods are investigated which allow to symmetrize the flow in front of the air intake again and, thereto, homogenize the flow at the aerodynamic interface plane. In this work, the feasibility of using particle swarm optimization even for challenging flow configurations and high performance computed CFD simulations is addressed. The special case of active flow suction in front of the air intake compression bump is considered. For a geometrically predefined blowing and suction area, air flow blowing and suction parameters have to be determined. An optimization framework is used to find the best possible solution for the geometrically constraint active controlled flow case. Beside the technical part this work has also the objective to contribute to the discussion about the necessary framework for active flow control.

1. Introduction

Next-generation combat aircraft will operate in very complicated environments, in particular within fast developing electronic warfare supporting air-to-air long range missiles. New radar systems require as a counteract superior stealth technologies, which are crucial for the survivability of combat aircraft. As a consequence, strong design rules for aircraft planform shapes have to be applied to minimize radar cross section (RCS). Each part of a fighter aircraft is affected, especially, the design of engine air intake shapes due to the necessity to reduce unnecessary edges and gaps if possible. The most critical part of the classical Pitot-type air intake is the boundary layer diverter, which increases the radar cross section significantly. Such a component has to be avoided, since in the gap between the boundary layer dividing flap and the fuselage the incoming radar radiance is quite strong reflected. Thus, air intake technologies, enabling less radar cross-section and maintaining good pressure recovery performance, have to be investigated. Although certain materials promise to provide RCS solutions, geometrical constraints are hindering. Therefore, alternatives to Pitot intakes have to be considered as replacement of diverter-based inlet systems. Here, compression-bump engine air intakes come into play which feature a three-dimensional geometrically fixed bump-like surface. The special challenge for fighter aircraft engine air intake design is to provide high intake performance for a wide range of maneuvers and flight Mach numbers from sub- to supersonic flows. Latter flow regime is the reason why such engine intakes are called diverterless supersonic intakes (DSI). Besides high total pressure recovery, flow distortion and other beneficial flow characteristics, these intakes have also gained significant importance in aircraft intake design due to weight reduction, less components and reduced maintenance efforts as compared to other conventional intakes^[13].

The integration of a DSI requires a well-designed compression bump surface, which provides boundary layer (BL) diversion and ensures a smooth flow inside the intake duct. The bump surface, along with an adapted inlet cowl design is found to be instrumental in diverting the upstream BL and creating air compression for the inlet system^[4]. By displacing the incoming boundary layer so far outwards that only high momentum flow enters the intake duct, they are able to deliver high total pressure recovery at the aerodynamic interface plane to the engine. Unfortunately, the physics of compression bump intake flows is getting more and more complicated once unsteady high Mach number flow effects occur. Over the entire flow range to be relevant to fighter aircraft, the complex flow physics is not completely understood^[10]. In order to explain occurring flow phenomena and extend existing compression bump design rules, the DLR has developed a generic compression bump air intake for further studies in the framework of the DLR projects DIABOLO and WINGMATES where focus is laid on the overall design of combat aircraft systems. Herein, aircraft related design methods, special numerical simulation software and experimental validation technologies are developed, whose capabilities and performance are verified and demonstrated in the development of the DLR future fighter demonstrator (FFD)^[11]. In this context, developing an efficient and optimized intake for supersonic fighter aircraft is a highly challenging and complex undertaking in industrial-related aircraft research projects[16] and requires successful iterative cooperation of highly skilled engineers from various disciplines, which include but are not limited to: aerodynamics, design, power plant and structure.

For the investigation and analysis of intake related aerodynamic flow phenomena, a generic diverterless supersonic compression bump air intake was designed with the focus on aerodynamics in the compression bump region and inside the intake duct up to the AIP, see^[9]. The resulting generic intake model was used, a research platform in experimental wind tunnel studies and associated CFD simulation campaigns under widely varying flow conditions. It has been observed that with not only increasing angles of attack (AoA) but also angles of side slip (AoS) the performance of the intake is rapidly decreasing, leading to higher distortion, swirl and also total pressure recovery losses at the aerodynamic interface plane (AIP) to the engine. Thus, in this numerical simulation study, controlled air flow (suction / blowing) is used to redirect the asymmetrically onflowing air in front of the air intake, trying to correct the unfavourable flow situation occurring at high angles of attack and aircraft side slip. In this investigation, three slit-like air vents are artificially incorporated as numerical boundary condition at the side wall of the generic fuselage model. The three slits are placed with a lateral offset in front of the compression bump. The chosen positions are first estimations and no special pre-simulations were performed, since in this study the primal objective has been to develop and integrate optimization techniques in the CFD simulation process chain. In order to gain the most effective air-suction boundary flow conditions for achieving the most homogeneous and performing onflow conditions at the AIP, an advanced particle swarm optimization (PSO) method has been applied. This AFC optimisation study concentrates on design Mach number flow of 1.8, and an AoA of 16° and an AoS of 10°. Based on the PSO simulation results, the investigation concentrates on the potentials of this kind of active flow control.

2. The Compression Bump Intake Model

The DSI concept promises to achieve low-loss pre-compression in an induced conical flow field at the compression bump, the resulting lateral static pressure gradient and the forward swept cowl synergetically achieve diversion of the BL fluid and, thus, make a diverter or BL bleed system redundant. The DSI concept model, created at DLR, was build to perform aerodynamic analysis of a realistic supersonic tactical aircraft intake. The basic geometrical shape was based on an analytical definition of a first bump segment published by Seddon and Goldsmith 1999^[13] and GARTEUR TP 129^[8]. The design Mach number was 1.8, the targeted original engine intake massflow was 154 kg/s. With these key parameters the basic dimensions were fixed. The key to making the DSI highly efficient was to optimize the shape of the bump geometry together with the cowl and duct, and to correctly position the bump relative to the duct opening. This also involved a complex optimization process^[3]. In fact, the demand for low radar cross-section values as a major constraint was increasing the challenge to achieve a well operating aerodynamic compression bump design. This demand led to the constraint to enforce a trapezoidal intake shape (view from the front), a parallel alignment of the outer surfaces and, furthermore, an edge parallelity of the cowl lips to wing leading edges and side rudder edges wuth respect to their plan form angles. Moreover, RCS constraints are affecting the shape of the intake channel directly, because the front view directly on the first compressor stage has to be avoided. Since the bump is covering the engine only partly, a S-shape intake channel design had to be realized to hide the engine completely. However, since the engine air intake channel had also the function to act as an flow diffusor, it had to be carefully designed in order to prevent losses in momentum, respectively total pressure^[7].

An important decision made was to investigate the flow at a belly engine intake, which can often be found at single engine fighter aircraft. As a consequence, the wings, the rear fuselage and the tailplane do not have any relevance to this kind of engine intake flow study, so not a complete aircraft had finally be designed: in fact, only the first half of the generic aircraft was modelled. To simplify the configuration, the fuselage behind the canopy and cockpit section was

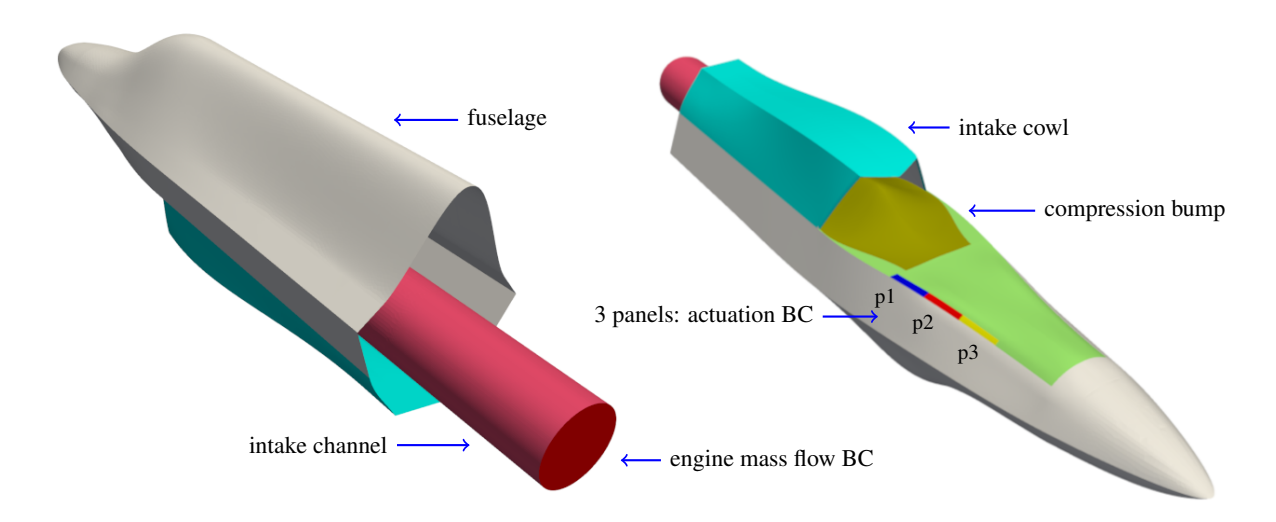


Figure 1: CAD views on the generic aircraft fuselage part with compression bump, intake cowl and channel, actuation panels and engine mass flow boundary part

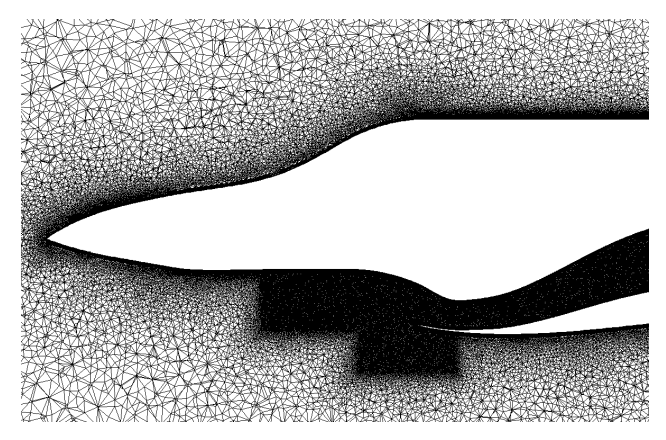
straightly extruded and integrated in one fuselage part. The new rear cross-sectional profile had the sole purpose of enhancing stability of the numerical simulation. The fuselage itself was taken from a generic fourth generation fighter aircraft, the nose section has been slightly stretched to extend the nearly flat surface in front of the intake to enable the generation of a fully developed boundary layer flow. Although quite generic, this allows for better investigations of the flow physical mechanism occurring at the compression bump intake. Further details of the design can be found in [9]. A cad view on the model is shown in Figure 1, in which the main parts of the configuration are assigned. In particular, the compression bump, the intake cowl and the active flow control panels are of special interest in this study. Finally, it has to be remarked, that the model was down-scaled to size suitable for wind tunnel testing.

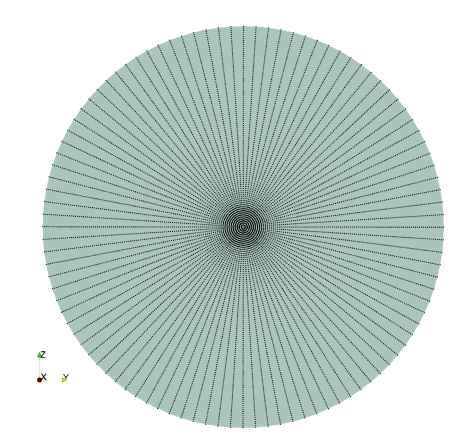
3. Numerical Flow Simulation Setup and the Optimization Problem

Before the CFD results can be discussed, the numerical setup of this study is explained. It starts with the grid generation study, followed by the description of the flow solver settings and finalized by the flow case selection.

3.1 Grid Generation

The numerical mesh is created with the commercial software "Centaur" by CentaurSoft. The surface of the combat aircraft model is discretized by triangles, followed by structured layers of prismatic elements, for a better spatial resolution of the boundary layer developing along the viscous walls, and unstructured tetrahedral elements for the remaining volume part of the flow domain. However, the height of the prismatic layer is not locally adjusted to the actual height of the local boundary layer. Consequently, several flow features such as vortices and shocks protrude into and out of the border between structured and unstructured elements. Since the vortex and shock detection algorithms are applied to the numerical data, the CFD demands a certain quality of the discretized gradients, thus a sufficiently fine grid resolution is necessary. Additional requirements are formulated for the quality of the elements. As a matter of fact, the current solution-based automatic grid adaptation of the CFD solver is not capable of pure isotropic, but only a mixture of isotropic and edge-based refinement. However, the consequence of edge-based refinement is that the element skewness increases with each adaptation step. After multiple adaptation iteration, this leads to anisotropic transport and decay of turbulence, which introduces a systematic error. The impact of this error can be small for many flow cases, nevertheless it should be considered when investigating vortical flows and shocks. Therefore, manual isotropic refinement was applied in this study, which eventually led to a high number of elements. In total, the numerical mesh consists of $38 \cdot 10^6$ points, which feature $97 \cdot 10^6$ cells. Of those, $34 \cdot 10^6$ are unstructured tetrahedral and $63 \cdot 10^6$ are structured prismatic volume elements, which are aligned in 36 layers. Last but not least, the surface of the DLR FFD compression bump model is discretized by $1.8 \cdot 10^6$ triangles. An impression of the refinement regions, the grid density but also the rake-like placement of 9901 sensor points at the AIP is delivered in Fig. 2.





(a) Cutting plane through the hybrid prismatic - tetrahedral CFD volume grid, high resolution grid regions are appearing more black.

(b) Distribution of sensor points (black dots) at the AIP for evaluation of the objective function.

Figure 2: Generic aircraft and intake flow configuration, CFD grid and AIP sensor points

3.2 Flow Solver, Flow and Boundary Conditions

The flow around the generic compression-bump engine air intake configuration is numerically investigated performing steady Reynolds-Averaged Navier-Stokes (RANS) simulations. The calculations were conducted on a Linux cluster using the DLR compressible finite volume solver TAU^[12]. The code uses a second order spatial and temporal discretization, it has been well validated by a variety of experimental and numerical validation campaigns and is state of the art in regard to performance, efficiency and accuracy. Different numerical acceleration techniques can be used. The flux splitting technique permits to perform inner sub-iterations for simulation speed up. In the current simulation campaign, the AUSMDV flux splitting scheme was applied to calculate upwind fluxes, the backward-Euler scheme as relaxation solver, gradients were reconstructed by using Green-Gauss scheme. In addition, implicit residual averaging and a 3-w multigrid cycle were performed to further accelerate the CFD calculations. Modeling of turbulence, in particular for flow situations with shocks and flow separation, is still challenging. Here, the one-equation Spalart-Allmaras turbulence model with the negative formulation and rotation correction was applied, since this model is able to deliver a good representation of shocks and wall shear stresses and has the capability to deliver reasonable results also for separated flows. It is also a good compromise in regard to computational effort. In the calculations, the CFL number was set to 0.2 due to stability reasons. More than 600000 iterations were computed in order to achieve a residual decline of alt least four orders of magnitude.

In the present work, only the supersonic flow case with a Mach number of 1.8 was investigated, the associated flow parameters were set as farfield condition. The small strips in front of the compression bump were treated as actuation type boundary condition, all other surfaces were treated as turbulent viscous walls. At the end of the intake channel the TAU fixed engine-mass-flow boundary conditions was used, here the mass flow was set to 1 kg/s (wind tunnel model scale). For details of this actuation boundary condition in the TAU code $\sec^{[6]}$. An initial simulation matrix was set up, varying the angle of attack (0°, 6°) and the side slip angle (0°, 10°) in order to get performance reference values for comparison. The active flow control optimisation was performed for an AoA of 6° and a side slip angle of 10°. It has to be remarked that in this study the flow of the scaled wind tunnel model was investigated in order to gain flow improvements to be further tested in future wind tunnel test campaigns. More details to the simulation settings can be found in Table 1.

Table 1: Flow parameters for the supersonic flow case - wind tunnel scale.

Mach number	$M_{\infty} = 1.8$
reference pressure	29.0 kPa
reference density	$0.3652 \frac{kg}{m^3}$
reference velocity	534.1 m/s
Reynolds length	0.2625 m
Reynolds number	$4.502 \cdot 10^6$
BC engine mass inflow	$\dot{m} = 1 \frac{kg}{s}$

3.3 Flow at the AIP as the Targeted Optimization Problem

Before going into the details of the particle swarm optimization algorithm, a brief view on the specific performance reducing flow structures at the intake compression bump and at the AIP is taken. Thereto, the flow situations at the Mach number of 1.8, the AoA of 6° and for the two angles of side slip, AoS 0° and AoS 10°, are investigated. Impression of the resulting flow fields are given in the Figures 3, 4a and 4b. In the first picture, for the given angle of attack even the no-side-slip flow case exhibits a strong dominating shock structure, visualised by the gradient of total pressure losses on the symmetry mid-plane. In particular, the terminal shock at the compression bump is so strong that a huge flow separation is initiated at the cowl lip, leading to a separation bubble far reaching into the intake duct. The Cp distribution on the fuselage is indicating the vortical spillage flow caused by the flow compression and the bump-shape induced pressure gradient in sidewards direction.

The second and third images, 4a and 4b, show the fuselage in upside-down position (used in all fuselage viewings), the slightly elevated front view allows to look partially into the intake. For both side slip cases, flow separation, resulting vortices and the surface pressure distribution are depicted. As expected, it is obvious that the flow symmetry of the side slip 0° case is massively disturbed in the AoS 10° case. Intake cowl vortices and the flow separation structure at the compression bump induced by the final compression shock are reflecting the asymmetric onflow situation. In particular, this leads to more pronounced separated vortical flows at the lee-side of the intake cowl. Since the flow-separation topology starts to change at the forefront of the compression bump and, then later passes into the intake channel, this was the reason to place the three active flow control panels at the described positions as a best guess. For

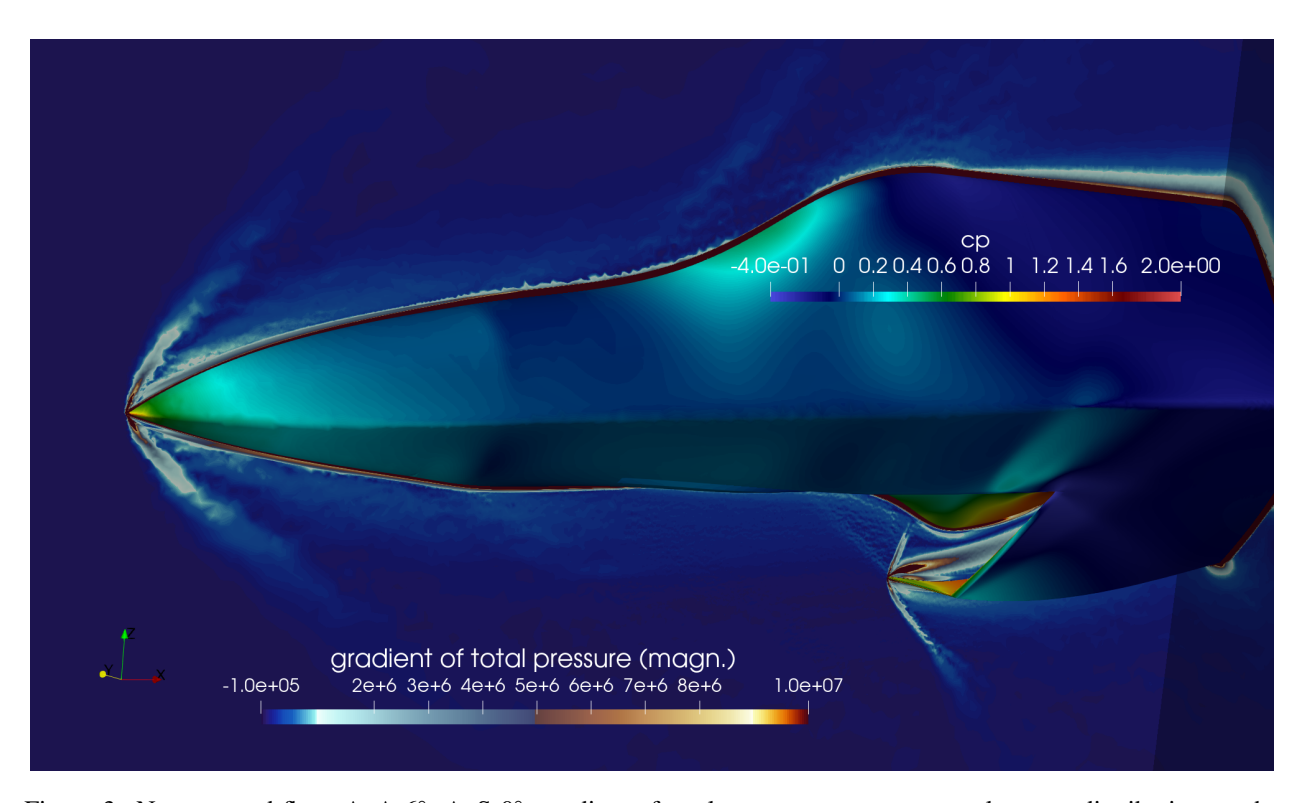
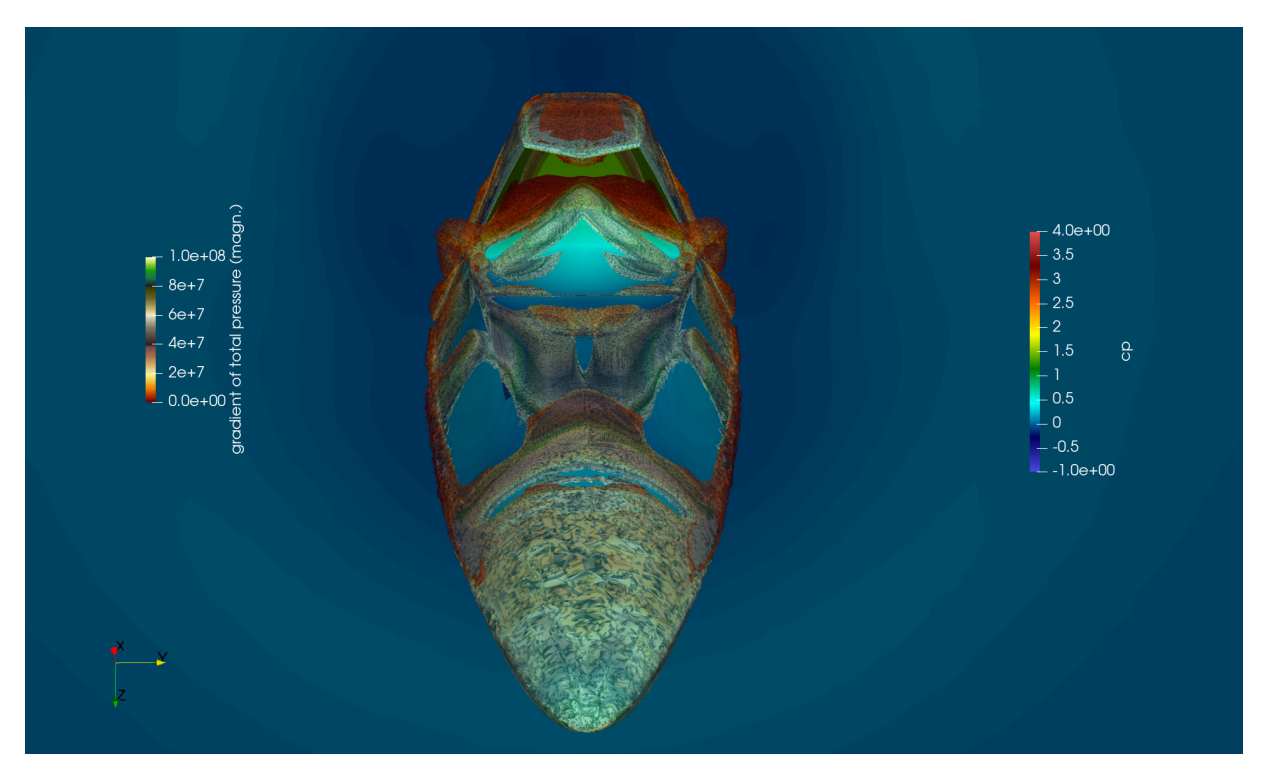
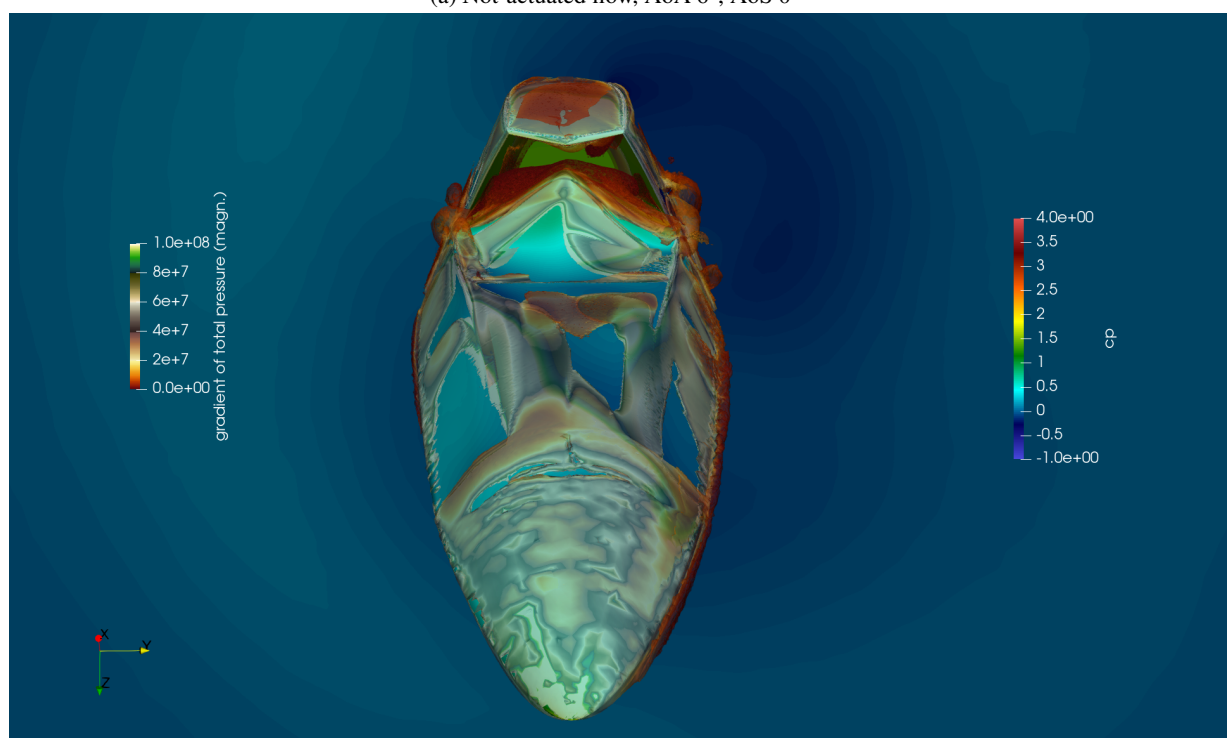


Figure 3: Not-actuated flow, AoA 6° , AoS 0° , gradient of total pressure on symmetry plane, cp distribution on the fuselage

the engine and, subsequently, the fighter performance, the flow situation at the AIP, in particular the total pressure loss distribution, is essential. Here, a completely different total pressure loss topology can be observed when comparing the Figures 5a and 5b: The axisymmetric double total-pressure loss extremum topology has changed to a twisted one, and the loss level is higher. Besides the higher losses this is crucial, because potential stall-minimizing or -preventing flow devices, i.e. vanes, would now be badly positioned. Therefore, the optimization objective is to achieve a more symmetrized onflow situation at the AIP by applying active flow control by steady blowing or suction. And the idea is that the applied optimization technique decides what kind of actuation is best.

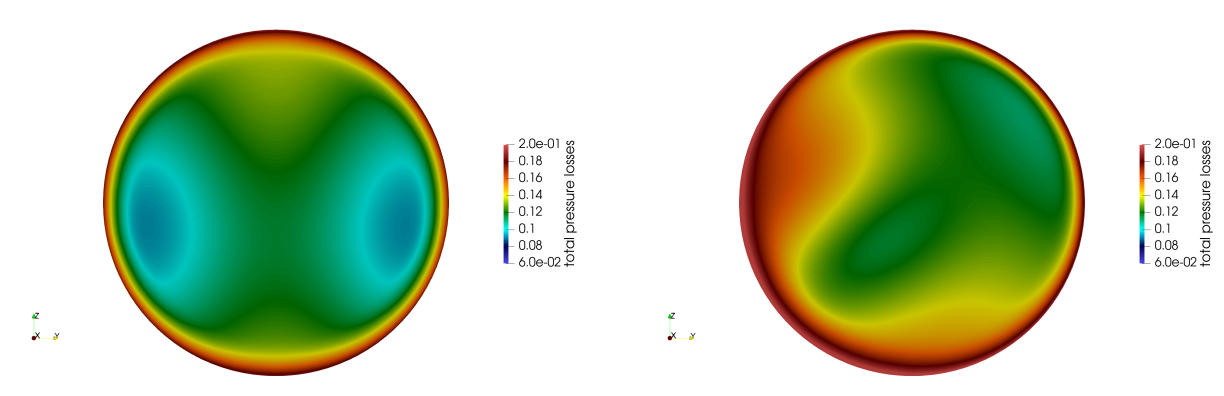


(a) Not-actuated flow, AoA $6^{\circ},$ AoS 0°



(b) Not-actuated flow, AoA $6^{\circ},$ AoS 10°

Figure 4: Upside-down fuselage, front view, flow separation and vortices at Mach 1.8, different slip angles



(a) Not-actuated flow, AoA 6°, AoS 0°, total pressure losses

(b) Not-actuated flow, AoA 6°, AoS 10°, total pressure losses

Figure 5: Total pressure losses at the AIP for the Mach 1.8 flow cases with different AoA and AoS

4. Optimization using a Particle Swarm Algorithm

As mentioned above, the feasibility of using PSO for high fidelity CFD is addressed. Therefore, in brief a general introduction of PSO is given. Thereafter, the specifics of the considered flow case are explained.

4.1 Particle Swarm Optimization

Particle Swarm Optimization is a computational technique that harnesses the collective intelligence of natural organisms to tackle optimization challenges. It is inspired by the cooperative behaviour of social animals like birds, ants, or fish. By imitating the intelligent collective behaviour of these swarms, particles share information about their environment to benefit the swarm^[5]. In the computational context it means that PSO consists of a swarm of generic particles, each representing a prospective solution to an optimization problem. These particles explore the solution space by adjusting their positions in the parameter space based on their own experiences and the successes of their neighbours. The primary goal of PSO is to find the global optimum of a given fitness (objective) function. This is achieved through the collective movement of particles towards areas of the solution space that offer better outcomes, as determined by the fitness function.

PSO is an efficient optimization procedure that starts with randomly positioned particles and iteratively updates their positions by considering both individual and collective discoveries, ultimately navigating towards the optimal solution. PSO is a flexible and easy-to-implement algorithm that does not require hyper parameter tuning. Each particle i in the swarm has a position, velocity, and fitness value. The position \vec{X}^i represents the parameter set that generates a certain solution of the function $f(\vec{X}^i)$, the velocity \vec{V}^i indicates the direction and speed of movement (from a start parameter set to a new one), and the fitness value, the value of $f(\vec{X}^i[t])$ at the current step t, measures how good the solution is. Particles keep track of their personal best positions \vec{P}_{Best}^i and the global best position \vec{g}_{Best} at the current step t, which guide the swarm's movement towards optimal solutions. The algorithm updates each particle's velocity and position based on a combination of its current velocity, the distance to its personal best position, and the distance to the global best position. So particles dynamically adjust their velocity and position based on \vec{P}_{Best}^i and \vec{g}_{Best}^i , which leads to exploration and exploitation of the search-space.

The PSO algorithm starts with an initial phase: Particles are initially scattered randomly within the problem space. This randomness ensures a broad exploration from the outset. Every particle is initially assigned a random velocity, directing its movement in the search space. This velocity is crucial for the dynamic adjustment of particle positions over iterations. Then, the iterative part of the optimization process follows: A velocity update has to be calculated, thereto at each iteration, the particle velocity is adjusted using the equation:

$$\vec{V}^{i}[t+1] = w * \vec{V}^{i}[t] + c_{1} * r_{1} * \left(\overrightarrow{p}_{Best}^{i}[t] - \vec{X}^{i}[t]\right) + c_{2} * r_{2} * \left(\overrightarrow{g}_{Best}[t] - \vec{X}^{i}[t]\right). \tag{1}$$

This formula incorporates the following constants which are the PSO control parameters: the inertia weight constant w, the cognitive coefficient c_1 and the social coefficient c_2 . Furthermore, the particle personal's best-known position $\overrightarrow{p}_{Best}^i$, and the swarm's global best-known position $\overrightarrow{g}_{Best}$ have to be calculated at each step t. The inertia weight constant w governs the particle momentum, balancing global and local exploration. It is chosen between 0 and 1 and determines how much the particle should keep on with its previous velocity, i.e., speed and direction of the search. A higher weight promotes global exploration, while a lower weight favors local exploitation. The parameters c_1 and c_2 controls how the

weight should be distributed between refining the search result of the particle itself and recognizing the search result of the swarm. Therewith, these parameters control the trade off between exploration and exploitation and they determine the influence of a particle's personal best and the global best on its velocity. Higher values of c_1 enforce individual learning, while higher values of c_2 promote group learning and exploration, which means for the particle movement: the cognitive coefficient c_1 reflects the particle's tendency to return to its personal best position, encouraging individual learning, whilst the social coefficient c_2 indicates the influence of the swarm's best-known position on the particle, fostering social learning and collaboration. Both together are blending the particle's historical data. Often c_1 and c_2 are set equal to 2.0 (as here), other settings can also be found in literature^[15], but usually c_1 equals to c_2 and ranges from [0,4]. $\overrightarrow{p}_{Best}^i$ is the position that gives the best value ever explored by particle i and $\overrightarrow{g}_{Best}$ is that best explored by all the particles in the swarm. The positions $\overrightarrow{p}_{Best}^i[t]$ and $\overrightarrow{g}_{Best}[t]$ are updated in each iteration $t \to t + 1$ to reflect the best position ever found so far. A further exploration, reflecting a kind of random distraction, is enabled by using the coefficients c_1 and c_2 , which are random numbers between 0 and 1. Due to this random distraction, running into local minima can almost be prevented by widening the search space^[1].

The most important property of the PSO algorithm, that distinguishes it from other optimization algorithms, is that it does not depend on the gradient of the objective function. In gradient descent, it is looked for the minimum of a function $f(\vec{X}^i)$ by moving \vec{X} to the direction of $-gradf(\vec{X}^i)$ where locally the function is going down the fastest. However, to find the global minima or maxima of a given quite complex objective fitness function can be challenging for gradient based methods when such a function has to be differentiated. In contrast, the PSO algorithm's ability to operate without the need for gradient information (gradient-free), means, that how a particle i at the position \vec{X}^i at the moment t moves, does not depend on which direction is "down hill", instead, it only depends on at which positions are \vec{P}_{Best}^i and \vec{g}_{Best} pointing. This makes PSO particularly suitable if differentiating is difficult or not possible. The side effect is also that a PSO algorithm can easily be parallelized which makes it suitable for a wide array of optimization problems.

Now, following the velocity update with a virtual temporal step t (unit value), the particle position is updated to:

$$\vec{X}^{i}[t+1] = \vec{X}^{i}[t] + \vec{V}^{i}[t+1]t, \qquad (2)$$

moving it closer to the optimal solution based on the newly calculated velocity. The swarm's collaborative movement, guided by both personal and global best positions, enables particles to explore and exploit the problem space effectively. This dual influence helps the swarm to converge towards the optimal solution over iterations. The process is repeated until a stopping criterion is fulfilled, such as reaching a maximum number of iterations or finding a satisfactory solution. This iterative process ensures that PSO can find solutions efficiently across various problem spaces, it should convergence towards an optimal solution.

The swarm size and topology are additional factors which are important for the swarm dynamics and, therewith, for the PSO efficiency^[1]. First, the swarm and neighbourhood size, which affects the diversity and convergence speed of the swarm. Larger swarms cover more search space but increase computational complexity. The neighbourhood size dictates the extent of information sharing among particles, influencing the convergence behaviour of the swarm. Second, the structure of the swarm's information-sharing network significantly affects the search process. There are two common networks: the star (global best), in which every particle is connected to every other particle, promoting rapid information dissemination but risking premature convergence; or the ring network (local best), in which particles are only connected to their immediate neighbors, which slows down the convergence but enhances exploration and prevents premature convergence. In most cases the global best approach is taken, as here in in this work.

Unfortunately, the size of the swarm, respectively the number of particles, and the number of iterations are crucial parameters that need to be optimized for each problem. A smaller swarm with more iterations might be more computationally efficient, while a larger swarm could potentially explore the search space more thoroughly but at higher computational costs. Guidelines found in literature propose a balanced approach with 20 to 40 particles and 1000 to 2000 iterations as a good starting point, combining efficiency with accuracy. For a CFD based optimization, however, this high number of iterations is, in most cases, not possible, therefore modifications^[14] or adaptive strategies are needed: Given the sensitivity of PSO's performance to its parameters, employing adaptive or self-tuning strategies that adjust the parameters based on feedback from the optimization process can significantly enhance the algorithm's effectiveness^[2]. This could involve dynamically changing the inertia weight or the cognitive and social coefficients.

4.2 CFD PSO Position Vector

A mentioned above, the starting point of the PSO algorithm is the definition of the position vectors of the particles. In this case, each particle position vector contains the distinct active flow control variable values which ares defining the numerical flow simulation results. Such a vector could be understood as the genetic information of a particle within a genetic algorithm approach. In Table 2, the bounds of the variables of the actuation boundary condition of TAU are

listed. These are the ranges in which the PSO algorithm can change the values. It starts with a random set out of these ranges. For each of the three panels, the same bounds were used.

Since this is a first try, it is highly plausible that better bounds could lead to better results, in fact, this work is a

actuation boundary condition	subtype standard
actuation direction (x,y,z)	[0.2, 1.0], [-0.4, 0.6], [-0.2, 0.4]
jet fluid pressure	[25000, 29000]
jet fluid Mach number	[0.6, 0.9]
iet diameter	[0.008_0.014]

Table 2: Active flow control variables - range of bound for all AFC panels

feasibility study. It has also to be remarked that the positioning of the actuation panels itself was not optimized, this is planned as part of future engineering work. Now, the optimization objective function and the associated evaluation criteria of the CFD flow case has to be explained.

4.3 Optimization Objective and Evaluation Criteria

The overall optimization objective of this AFC approach is to improve the intake air flow to guarantee a high performing engine behaviour delivering an efficient aircraft propulsion even for challenging maneuver flights. This depends strongly on the flow at the AIP. In order to get the essential information about the flow at the AIP in wind tunnel experiments special flow rakes are used, specifications can be found in the book of Seddon^[13]. In contrast to experiments where the instrumentation of a rake has to be limited in order to prevent flow blockage, in the CFD approach a high number of virtual sensor point can be used to gain the essential flow information. In Figure 2b the sensor points are depicted as black dots. Here, 100 rakes each with 100 evenly distributed sensors virtually defined and covering the circular AIP having a diameter of 0.075 m. The most interesting quantity for the aircraft designer and especially for the engine manufacturer is the total pressure recovery, respectively the accumulated total pressure losses at the AIP. A rule of thumb from engine manufacturers is that intake losses are affecting the engine performance in quadratic order, i.e. for 2 % of air intake and intake duct channel losses round about 4 % of engine performance are lost. Therefore, the ratio of the total pressure at the AIP to the onflow total pressure, is, of course, a main evaluation quantity,

$$\Pi = \frac{p_{tot,AIP}}{p_{tot,\infty}},\tag{3}$$

and, thus, an essential measure for the engine air intake performance. Here, in this work, a loss formulation is chosen:

$$P_{tot,loss} = 1.0 - \frac{p_{tot,AIP}}{p_{tot,\infty}},\tag{4}$$

The homogeneity of the engine onflow is a further major criterion for the design of air intakes and ram air diffusor intake channels. In fact, an even distribution of inflow velocity and pressure at the AIP is the essential and preferred objective in intake design^[13]. One possibility to evaluate the homogeneity of the flow is to use the total pressure sensor information to calculate the distortion coefficient DC(60). It is defined as

$$DC(60) := \frac{\bar{p}_t|_{360^{\circ}} - \bar{p}_t|_{60^{\circ}}}{\frac{1}{2}\bar{\rho}\bar{v}^2}.$$
 (5)

In this equation the $\bar{p}_t|_{360^\circ}$ is the averaged total pressure of the whole cross section, $\bar{p}_t|_{60^\circ}$ is the averaged total pressure of that specific cross-sectional 60°-area, where the absolute minimum of total pressure occurs. The difference is normalized by $\frac{1}{2}\bar{\rho}\bar{v}^2$, which is the averaged dynamic pressure over the whole cross sectional area. The type of averaging used depends on the type of rake and instrumentation. In this study area-averaging is applied. A DC(60)-value of zero would represent a homogeneous onflow, a higher value is indicating a greater inhomogeneity. It should be mentioned, that other cross-sectional angles than 60° can be used.

The uneven distribution of total pressure at the AIP may also be a result of a kind of cross flow leading to swirl, not only from a different level of momentum inflow but also from surface contouring. Therefore, an expression for AIP inplane cross flow has to be taken into account in engine air intake channel design. Accordingly, also a distortion criterion

$$\Psi := \frac{\sum A_i (\sqrt{v_r * v_r + v_\phi * v_\phi})_i}{\sum A_i (\sqrt{v_r * v_r + v_\phi * v_\phi + v_z * v_z})_i}.$$
 (6)

can be defined to evaluate the effect of highly curved compression bump intakes and intake channels, so the ratio Ψ of the area averaged in-plane velocity magnitude to the overall area-averaged velocity magnitude can be used to further quantify the flow inhomogeneity at the AIP.

However, the considered flow case showed a different behaviour in regard to the shape of the total pressure loss and flow distortion region. Instead of revealing only a single quite circular or slightly elliptical and compact concentrated loss region, an irregularly disfigured loss region occurs when increasing AoA and AoS. Thus, for the objective function a more general approach for evaluating the homogeneity of the total pressure at the AIP was developed: it is calculated how many sensor points measure values less than a specific threshold times the area averaged total pressure in comparison to the total number of sensor points:

$$P_{tot,hom} := \frac{no_sensors(p_t < 0.96 \cdot \bar{p}_t)}{nges_sensors}. \tag{7}$$

The threshold is set to 0.96 determined in pre-simulation studies.

The same approach is chosen for the assessment of the velocity swirl. Hereto, a special velocity swirl criterion is formulated, see eq. (8): The overall maximum of the cross flow velocity components is determined, then it is calculated how many sensor points show cross flow velocity components bigger than a threshold value of 0.4 times the maximum. This threshold has been estimated by investigating different flow cases:

$$\Psi_{cross} := \frac{no_sensors(V_{cross} > 0.4 \cdot V_{cross_max})}{nges_sensors}.$$
 (8)

The determination of the weight of the single contributors to get a suitable weighted objective function for performance studies could not be found in literature, hence, an own function was defined:

$$f(\vec{X}^i) := (0.6 \cdot P_{tot,loss} + 0.2 \cdot P_{tot,hom} + 0.2 \cdot \Psi_{cross})_{CFD \ solution(\vec{X}^i)}. \tag{9}$$

The input into equation (9) are the total pressure and distortion values stemming from the CFD solution generated based on the "genetic" information of the particle \vec{X}^i .

The PSO algorithm was applied, and in pre-tests runs it became clear very fast, that it was necessary to make adjustments to the pre-test runs. The decision to use an acceleration method was an essential step in regard to save costs: Here, based on experience, an exponential decrease of the inertia weight has been used to reduce the number of iterations needed for achieving a converged solution. Hence, with only 18 particles and after 11 generations of particle swarm movements a satisfying result could be achieved. It has to be remarked that the taken solution was not the overall-best, however, observations of intermediate results revealed that gain improvement was not high anymore and convergence was nearly achieved, thus, the optimization loop was stopped in order to save computational costs.

5. Analysing the PSO Flow Results

Now, the results of the flows with and without actuation are analyzed and compared against each other. The PSO algorithm has been applied for three different AFC, flow data listed in Table 3. Two essential observations can be made: Firstly, for each panel some range limits for the direction, Mach number, jet pressure and jet diameter are touched, which eventually mean that the full possible potential of the chosen AFC approach could not been achieved due to these limitations. Secondly, the type of actuation is changing in upstream direction from a weak sidewards-oriented air jet blowing to an upstream directed air suction.

actuation boundary condition panel 1 panel 2 panel 3 $(0.67\overline{77}, 0.6, 0.1320)$ (0.2, 0.2896, 0.4)(1.0, 0.201278, 0.4)actuation direction (x,y,z) 27390.7 jet fluid pressure [Pa] 25000 25000 jet fluid Mach number [-] 0.9 0.6064 0.6 0.008 0.014 jet diameter [m] 0.0097 resulting mass flow $\left[\frac{kg}{c}\right]$ 0.02421 0.03988 0.01823 AFC type weak sidewards pure suction upstream blowing directed suction

Table 3: Active flow control variable settings for all three AFC panels

To give a first impression of the overall flow topology, the separated and vortical flow field and the associated surface

pressure contour are visualized, see the Figures 6a and 6b. Obviously, the separated flow at the AFC panels is suppressed due to the partial blowing and suction of air flow. At the compression bump, a slightly shift of flow separation can be observed which affects the down-stream vortical flow in a smaller manner. The flow topology change is barely visible, thus, it has to be deduced that the best-guess placement of the actuation panels and their operational settings resulting from PSO can not deliver an essential performance gain. This is a strong indication, that more advanced flow analysis techniques, stability analysis, vorticity flux assessment or mode decomposition, are necessary in order to get the crucial flow sensitivity information which should result in a more beneficial AFC device placement. In fact, the dominant shock structure at the compression bump is so strong, that even the flow actuation is not be able to counteract its flow topology shaping dominance. One lesson might be, that an AFC device has to be placed directly upstream of the terminal shock.

As remarked, the active flow control effect is unfortunately very limited to the AFC panel region. However, the vortical flow at the compression bump and, hence, as a result, the flow within the intake duct is also effected, although weakly. The accumulating flow effects can be assessed at the AIP. Here, total pressure losses and flow field distortions are analysed and compared.

At first glance the total pressure loss distribution of the actuated flow case seems to be very similar to that of the not-actuated flow case, when comparing the illustration in Figure 7a with the image in Figure 5b. A very slight hue colour value change is indicating small differences, thus, a subtraction of the total pressure losses has been performed leading to a difference plot of total pressure loss shown in Figure 7b. Now, the small changes are quantified, they are mostly in the range of 1%, which means, that the AFC has a beneficial impact on the flow. However, the effect in regard to pressure recovery is not so strong that the effort of actually implementing an AFC system could be justified.

In the next two figures the flow distortion at the AIP is analysed, thereto, firstly, the distortion distribution of the actuated flow is calculated following equation (6) and depicted in Figure 8a, and secondly, the difference of the distortion between the actuated and non-actuated reference flow case, calculated and illustrated in Figure 8b. Again, a twisted double extremum topology is revealed, where the distortion extrema are closer together in comparison to the symmetric flow case of $AoA 6^{\circ}$, $AoS 0^{\circ}$. This distortion extrema vicinity will have an effect on the fitness values discussed now.

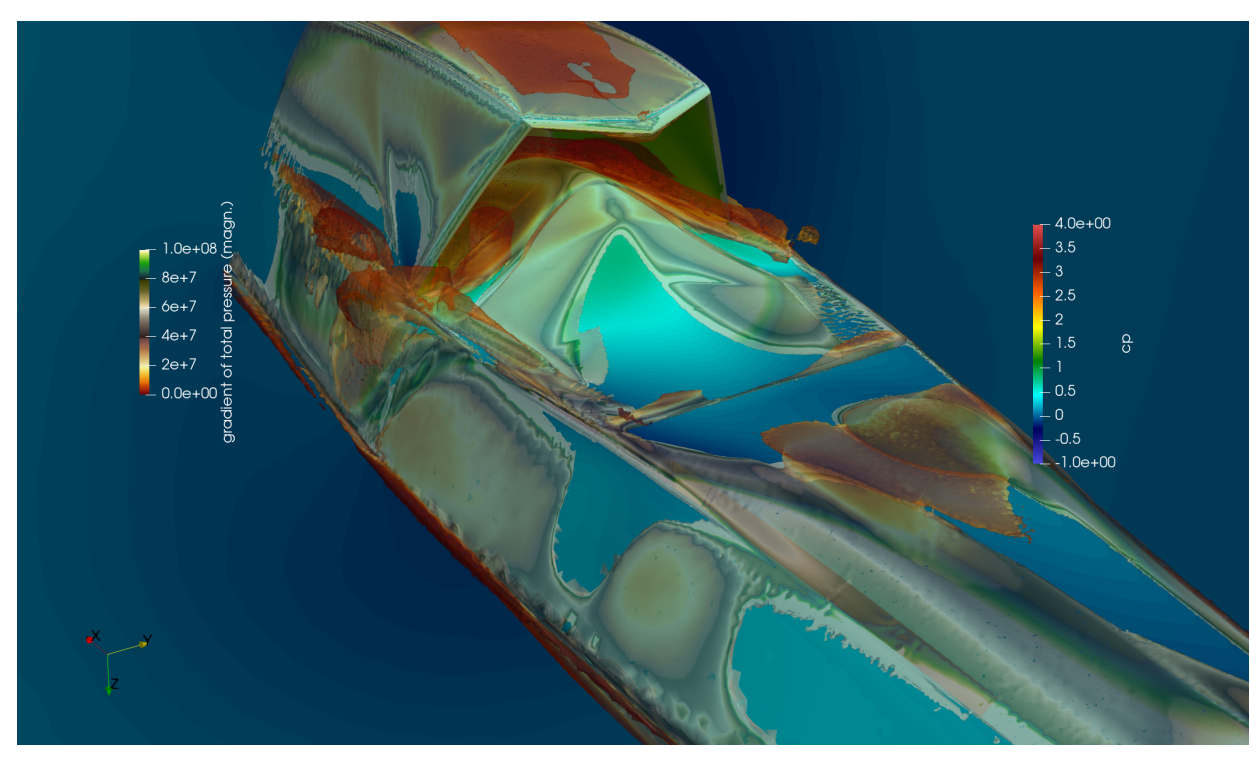
The quantitative comparison of the total pressure loss and distortion distribution has revealed that the AFC approach is able to generate an affect on the flow field at the AIP, despite the suboptimal AFC panel placement. Now, the point is reached to compare the AIP area-averaged evaluation values and the associated fitness values. In Table 4 this essential information is listed, which allows some crucial observations. Starting with the flow case without side slip angle: Here, the total pressure recovery is the best, showing the smallest total pressure loss, the best total pressure homogeneity and the smallest DC(60) value. However, the evaluation of the latter values can be misleading, because the flow field at the AIP reveals two not connected total pressure and flow field distortion extrema. In fact, the overall higher total pressure level affects the global pressure homogeneity positively (see eq. (7)). And more misleadingly: in regard to the DC(60) criterion, only one extrema is selected for evaluation due to small value variations. Thus, the velocity swirl criterion (see eq (8)) has to be considered, which, in fact, reveals a relatively bad value. Interestingly, this has a huge, crucial impact on the fitness value although it is low weighted (see eq. (9)): Since the flow case without side slip is the most worse of the evaluated flow case in regard to the fitness value, this exposes the weakness of the fitness function, and, in particular, this observation opens the discussion, how to formulate an appropriate objective function for the calculation of fitness values. Nevertheless, when comparing the evaluation values of the flow cases with side slip, both with and without actuation, all values show a slight improvement of the flow situation at the AIP, when the flow is actuated.

When reviewing the final achievements, then it can be stated that the PSO process chain is working and is able to

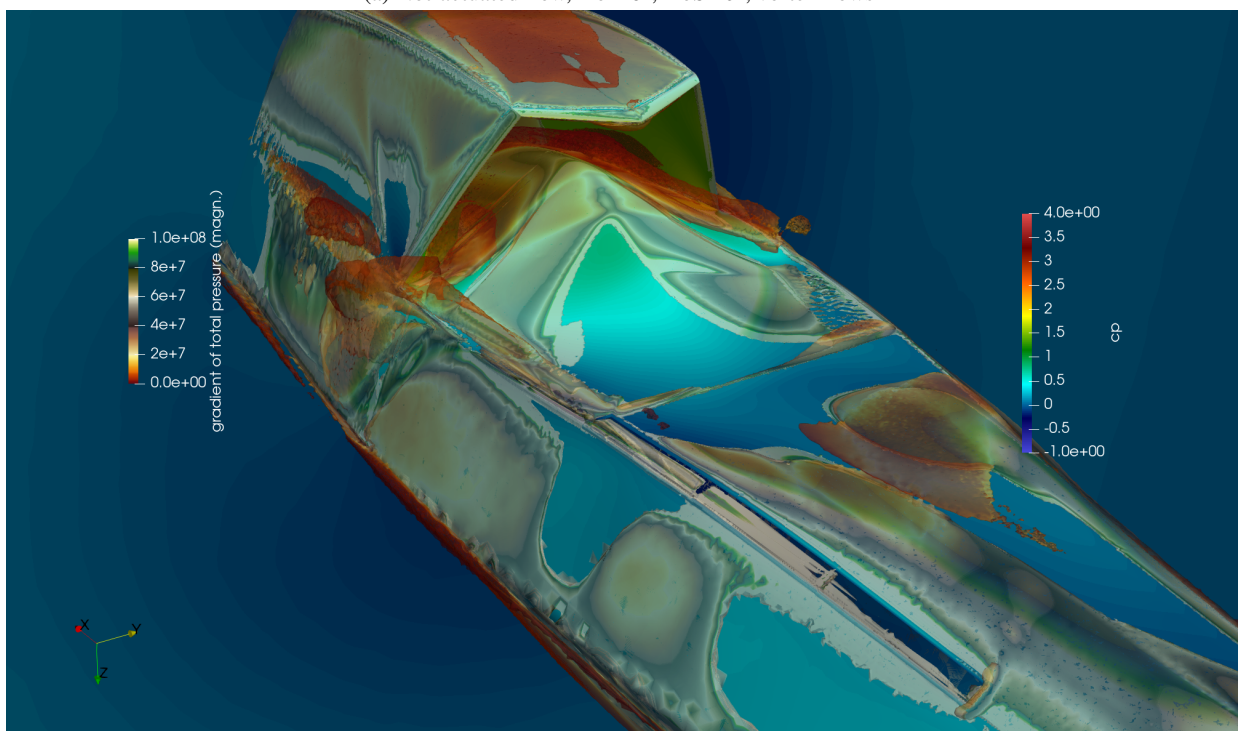
flowcase	no, 6°, 0°	no, 6°, 10°	AFC, 6°, 10°
$P_{tot,AIP}[kPa]$	146482.83	143249.93	144424.11
$P_{tot,loss,AIP}[-]$	0.1189	0.1346	0.1272
$DC(60)_{AIP}[-]$	0.1819	0.2061	0.1863
$P_{tot,hom,AIP}[-]$	0.03523	0.04932	0.04868
$\Psi_{AIP}[-]$	0.00378	0.02953	0.0276
$\Psi_{cross,AIP}[-]$	0.3898	0.22934	0.2021
fitness[-]	0.1563	0.1365	0.1265

Table 4: Summary of performance values of the test cases presented above

elaborate AFC parameters even for a given unfavourable AFC panel placement, leading to an improvement of the flow at the AIP. The benefits are not high and they would not justify an implementation of the presented approach. However, the main progress is that through this investigation it became clear that it is inevitable to rethink AFC approaches: without a sophisticated flow analysis framework around, flow control measures will fall short and won't be able to successfully enhance targeted aerodynamic, engine and flight related performances.

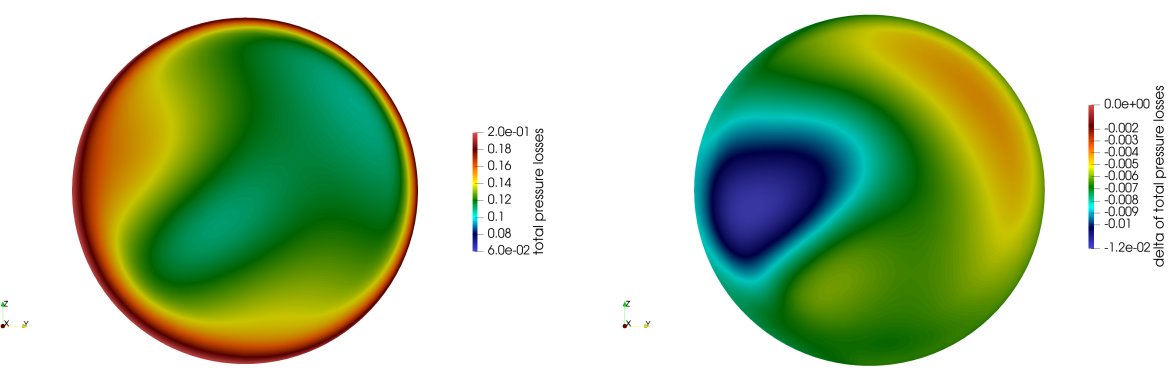


(a) Not-actuated flow, AoA 6° , AoS 10° , vortex flows



(b) Active flow control, AoA 6°, AoS 10°

Figure 6: Upside-down fuselage front view, flow separation and vortical flows at Mach 1.8, flow actuated and not



(a) Active flow control, total pressure losses

(b) No and active flow control, difference plot of total pressure losses

Figure 7: Total pressure losses at the AIP for the Mach 1.8 flow cases at AoA 6°, AoS 10°

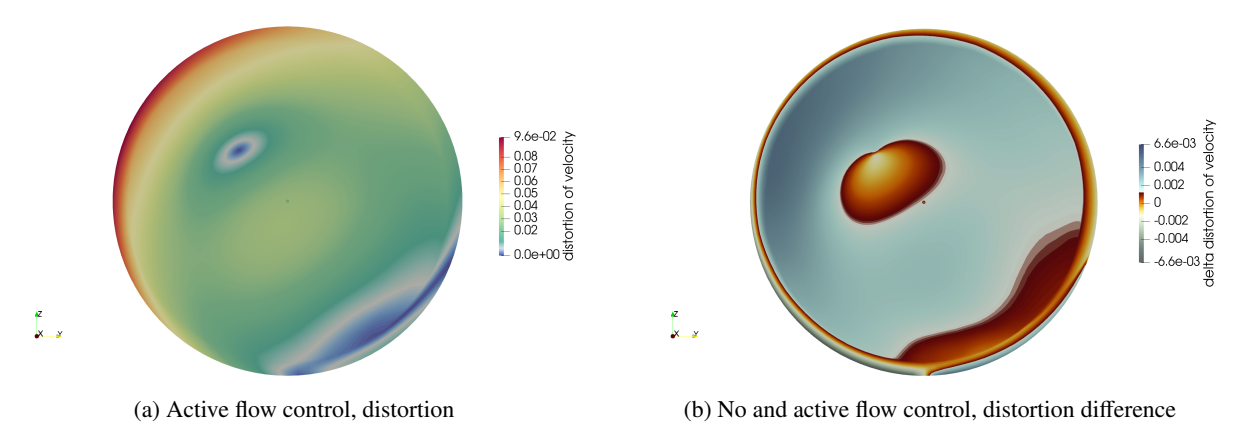


Figure 8: Distortion and its change at the AIP for the uncontrolled and controlled flow cases, AoA 6°, AoS 10°

6. Conclusion

The present work gives a brief introduction into the feasibility to apply active flow control techniques for the enhancement of the performance of compression bump engine air intakes. In particular, the focal point of the numerical flow simulation study was the development of a PSO process chain which shall allow for optimizing the active flow actuation parameters in order to improve the performance of the given intake under the difficult flight conditions of an angle of attack of 6° and side slip angle of 10°. The resulting flow at the interface to an engine shall be improved.

Despite the fact, that it could be shown that a slight performance gain in regard to the reduction of total pressure loss and flow distortion at the AIP could be achieved, it became clear, during the PSO simulation loops, that the chosen positions for the three active flow panels are not ideal, even not good guesses, as they should have been. In fact, the strong shock structure at the compression bump remains so dominating that the chosen AFC approach could not overcome its flow topology shaping dominance. The clear conclusion is that the presented active flow optimization process chain alone is not appropriate to handle those kinds of difficult flow problems. A flow sensitivity analysis, vorticity flux assessment and, perhaps, mode decomposition techniques have to be incorporated into the process chain in advance of the setup of active flow control devices and its optimization. Due to the presented results, the combination of compression-bump intake-shape, flow field stability and sensitivity analysis and active flow control optimization will be a point of future work in order to further increase the overall performance of this kind of engine intakes.

Acknowledgment

The authors acknowledge the scientific support of the projects "DIABOLO" and "WINGMATES" and support of the HPC resources provided by the German Aerospace Center (DLR). The HPC system CARO is partially funded by "Ministry of Science and Culture of Lower Saxony" and "Federal Ministry for Economic Affairs and Climate Action".

References

- [1] R.C. Eberhart and Y. Shi. "Comparing inertia weights and constriction factors in particle swarm optimization". In: *Proceedings of the 2000 Congress on Evolutionary Computation (CEC â00)*. Vol. 1. 2000, pp. 84–88. DOI: 10.1109/CEC.2000.870279.
- [2] Diogo Freitas, Luiz Guerreiro Lopes, and Fernando Morgado-Dias. "Particle Swarm Optimisation: A Historical Review Up to the Current Developments". In: *Entropy* 22.3 (2020). ISSN: 1099-4300. URL: https://www.mdpi.com/1099-4300/22/3/362.
- [3] J.W. Hamstra et al. *Development, verification & transition of an advanced engine inlet concept for combat aircraft application*. Tech. rep. Lockheed Martin Corporation, 2003.
- [4] J.W. Hamstra et al. *Transition Shoulder System and Method for Diverting Boundary Layer Air*. U.S. Patent No. 5, 749, 542, 12 May. 1998.
- [5] J. Kennedy and R.C. Eberhart. "Particle swarm optimization". In: *Proceedings of the International Conference on Neural Networks*. Vol. 4. 1995, pp. 1942–1948. DOI: 10.1109/ICNN.1995.488968.
- [6] Tobias Knopp. *The actuation boundary condition for flow control in the DLR TAU Code*. Tech. rep. 2011. URL: https://elib.dlr.de/71731/.
- [7] A.D. Gardner M. Rein M. Hannemann and St. Koch. *Design of a generic subsonic S-duct intake for studies on the effect of boundary layer ingestion*. Deutsches Zentrum für Luft- und Raumfahrt e.V Institute of Aerodynamics and Flow Technology, 2009.
- [8] P.G. Martin et al. A study of the aerodynamics of an intake bump compression surface at subsonic and supersonic speeds using cfd methods. Tech. rep. TP–129. The Group for Aeronautical Research and Technology in Europe (GARTEUR), 2001.
- [9] M. Rütten. "Flow Phenomena Resulting From a Compression-Bump Engine Air Intake". In: *AIAA SCITECH* 2025 Forum. 2025. DOI: 10.2514/6.2025-0881.
- [10] E.B. Saheby, X. Shen, and A.P Hays. "Design and performance study of a parametric diverterless supersonic inlet". In: *Proceedings of the Institution of Mechanical Engineers*. Vol. 234. Part G: Journal of Aerospace Engineering 2. 2020, pp. 470–489. DOI: 10.1177/0954410019875384.
- [11] A. Schuette and D. Hummel. "Impact of planform and control surfaces on the vortical flow topology and roll stability of a multi delta wing configuration". In: *Proceedings of the AIAA AVIATION 2022 Forum*. 2022. DOI: 10.2514/6.2022-3437.
- [12] D. Schwamborn et al. "Development of the TAU-Code for aerospace applications". In: *Proceedings of the 50th NAL International Conference on Aerospace Science and Technology*. Bangalore, India, June 2008.
- [13] J. Seddon and E.L. Goldsmith. *Intake Aerodynamics*. AIAA education series. American Institute of Aeronautics and Astronautics, 1999. ISBN: 9780632049639.
- [14] Y. Shi and R.C Eberhart. "A modified particle swarm optimizer". In: *Proceedings of the IEEE International Conferences on Evolutionary Computation*. 1998, pp. 69–73. DOI: 10.1109/ICEC.1998.699146.
- [15] Y. Shi and R.C Eberhart. "Parameter selection in particle swarm optimization". In: *Evolutionary Programming VII: Proc. EP 98.* Springer-Verlag, New York, 1998, pp. 591–6003.
- [16] M.R. Soltani and R. Askari. "On the Performance of a Body Integrated Diverterless Supersonic Inlet". In: *Aerospace Science and Technology* 91 (2019), pp. 525–538. ISSN: 1270-9638.